Astronomy & Astrophysics manuscript no. zhaohh
December 30, 2016
© ESO 2016

The X-ray view of black-hole candidate Swift J1842.5-1124 during its 2008 outburst

H.-H. Zhao[1], S.-S. Weng[1,2,⋆], J.-L. Qu[2], J.-P. Cai[1], Q.-R. Yuan[1]

[1]Department of Physics and Institute of Theoretical Physics, Nanjing Normal University, Nanjing 210023, China
[2]Laboratory for Particle Astrophysics, Institute of High Energy Physics, Beijing 100049, China

arXiv:1612.09110v1 [astro-ph.HE] 29 Dec 2016

Preprint online version: December 30, 2016

ABSTRACT

Context. The spectral and temporal evolution during X-ray outbursts give important clues on the accretion process and radiation mechanism in black-hole X-ray binaries (BH XRBs).
Aims. A set of *Swift* and *RXTE* observations were executed to monitor the 2008 outburst of the black-hole candidate Swift J1842.5-1124. We investigate these data to explore the accretion physics in BH XRBs.
Methods. We carry out a comprehensive spectral and timing analysis on all the available pointing observations, including fitting both X-ray spectra and power density spectra, measuring the optical and near-ultraviolet flux density. We also search for correlations among the spectral and timing parameters.
Results. The observed properties of Swift J1842.5-1124 are similar to other BH XRBs in many respects, for example the hardness-intensity diagram and hardness-rms diagram. The type-C quasi-periodic oscillations (QPOs) were observed as the source started to transit from the low-hard state to the high-soft state. The frequency of QPOs correlate with intensity and the hard component index, and anti-correlate with the hardness and the total fractional rms. These relations are consistent with the Lense-Thirring precession model. The estimated U-band flux changed with the X-ray flux, while the flux density at the V band remained 0.26 mJy. These results imply that the X-ray reprocessing or the tail of thermal emission from the outer disk contributes a significant fraction of the U-band radiation; alternatively, the companion star or the jet dominates the flux at longer wavelengths.

Key words. accretion, accretion discs — black hole physics — X-rays: binaries — X-rays: stars — X-rays: individual (Swift J1842.5-1124)

1. Introduction

In the Galaxy, X-ray emissions are dominated by accreting compact objects and isolated neutron stars (e.g. pulsars). Most black-hole X-ray binaries (BH XRBs) are transients, and more than one hundred outbursts are recorded in the vast database in approximately the past 20 years (see, e.g. Tetarenko et al. 2015; Corral-Santana et al. 2016). The phenomenology of the evolution of BH XRBs outbursts appears complex, and different state classifications have been proposed by different authors (e.g. see the review by Remillard & McClintock 2006; Zhang 2013). Based on the hardness and timing properties, the spectral states of BH XRBs can be distinguished into the low-hard state (LHS), the hard-intermediate state (HIMS), the soft-intermediate state (SIMS), and the high-soft state (HSS) (see, e.g. Belloni & Motta 2016).

Relationships among the spectral and timing parameters are crucial to the study of accretion flows in BH XRBs (e.g. Belloni et al. 2005; Miller et al. 2006; Ingram & Done 2011). Investigating the phase/time lag allows us to explore the connection between the accretion disk and the corona and jet (e.g. Qu et al. 2010; Altamirano & Méndez 2015; Reig & Kylafis 2015; Veledina et al. 2015). Three types of low frequency quasi-periodic oscillations (QPOs), i.e. type-A, type-B, and type-C QPOs, have been occasionally observed at different spectral states (e.g. Casella et al. 2005; Roy et al. 2011; Li et al. 2013). The study of low frequency QPOs provide an opportunity to understand accretion flows close to central black-holes (BHs). When sources transit from the HIMS to the SIMS, the type-C QPOs disappear and the type-B QPOs might be present in the power density spectra (PDSs) (Belloni & Motta 2016, and references therein). It is worth noting that the transition takes place with a minor change in hardness and sources cross the so-called jet line in the hardness-intensity diagram (HID) (e.g. Fender et al. 2004). The association of the type-B QPOs and the ejection of relativistic ballistic jets has been revealed in BH XRBs (e.g. Soleri et al. 2008; Kylafis & Belloni 2015). Various models taking instabilities and geometrical effects into account, have been proposed to explain the origin and the behaviour of QPOs in BH XRBs (e.g. Stella & Vietri 1998; Ingram et al. 2009; Varnière et al. 2012).

The disk instability model (DIM) is widely accepted as the explanation for outbursts in dwarf nova. The model has also been suggested to account for outbursts in X-ray transients, but in the meantime various deficiencies have been figured out (see the review by Lasota 2001). In order to reproduce the major observational phenomena, the DIM should take the irradiation effect and a transition to a radiatively inefficient accretion flow below a critical mass-transfer rate into account (e.g. King & Ritter 1998; Coriat et al. 2012). Irradiation by the central X-ray source is required to keep the outer disk hot and generate slow exponential decay light curves (e.g. Chen et al. 1997; Yan & Yu 2015). This scenario is supported by the correlation between the X-ray and the optical and near-ultraviolet (NUV) luminosities (van Paradijs & McClintock 1994; Rykoff et al. 2007).

⋆ E-mail: wengss@njnu.edu.cn

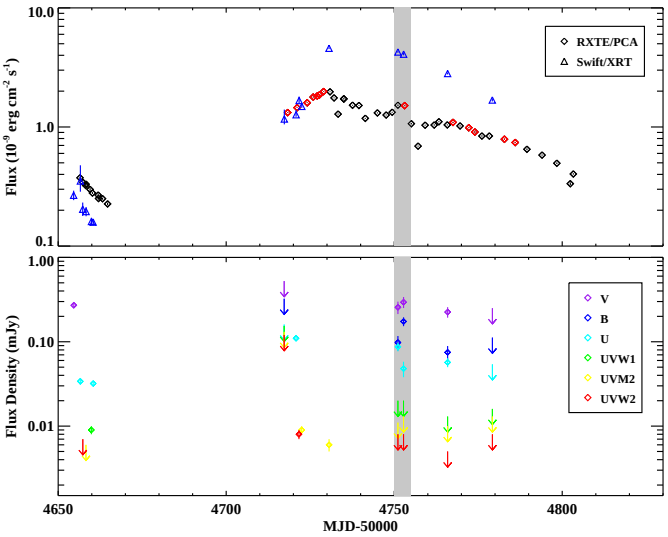

Fig. 1. X-ray (top panel, Tables 1 and 2) and optical and NUV light curves (bottom panel) for the 2008 outburst of Swift J1842.5-1124. The red symbols corresponds to the data in which QPOs were observed. Shaded areas indicate the period when the source took the excursion in the HID (Figure 2).

Recently, Weng & Zhang (2015) analysed the multiwavelength light curve evolution of Swift j1357.2-0933 during its 2011 outburst, and found that the X-ray reprocessing was negligible since the NUV luminosity was close to and even exceeded the X-ray luminosity at the times; however, the light curves displayed the typical near-exponential decay profile. This means that there is need for improvement in the current version of DIM, and the origins of NUV emission are diverse (i.e. stemming from the companion star, jet, the outer disk, etc).

Swift J1842.5-1124 was discovered on July 2008 by the *Swift*/BAT (Krimm et al. 2008). A series of *RXTE* and *Swift* observations were carried out to follow up the outburst. The multiband light curves had been presented in Krimm et al. (2013), and the hard X-ray peak preceded the soft X-ray peak by a few days, being consistent with those observed in other BH XRBs (e.g. Zhou et al. 2013). In addition, both spectral and temporal fittings were performed using a few individual observations (e.g. Markwardt et al. 2008). But there is still a lack of systematic study on the spectral and timing evolution during the 2008 outburst. In this work, we take a detailed analysis on both *RXTE* and *Swift* observations. The data reduction is described in next section, and the results are presented in Section 3. Since Swift J1842.5-1124 showed some common observed properties with other BH XRBs, it was recognized as a promising BH candidate. In Section 4, we discuss the analysis results and compare them with other BH XRBs. The summary follows in Section 5.

2. Observations and data reduction

Swift J1842.5-1124 triggered the *Swift*/BAT in 2008 July (Krimm et al. 2008), and was visited by *Swift* and *RXTE* on 16 and 49 occasions in 2008, respectively. The light curves for the activities are displayed in Figure 1.

2.1. Swift

The *Swift* Gamma Ray Burst Explorer carries three scientific instruments, including the Burst Alter Telescope (BAT), the X-ray Telescope (XRT), and the UV/Optical Telescope (UVOT) (Gehrels et al. 2004). Because of broadband coverage and scheduling flexibility, *Swift* is ideally suited to tracing outbursts of accreting X-ray binaries. Both the XRT and UVOT data are processed with the packages and tools available in HEASOFT version 6.17 in the standard way. The XRT operating mode switched between the photon counting (PC) and the windowed timing (WT) modes in order to minimize the pile-up effect. The raw data are performed for the initial event cleaning using the `xrtpipeline` script. The source spectra are extracted within a circle of radius 20 pixels centred at the nominal position of Swift J1842.5-1124 (R.A. = 18:42:17.45, decl. = -11:25:03.9, J2000) with `xselect`, while an annulus region with the radius of 20 and 40 pixels is adopted for background region. The ancillary response files are produced with task `xrtmkarf`, and the latest response files (v014) are taken from the CALDB database. We also rebin the spectra to have at least 20 counts per bin to enable the use of χ^2 statistics. Because there are calibration residuals at the energy below 0.6 keV for the WT mode data [1], the spectral fitting are restricted to the 0.6–10 keV band.

For the X-ray spectral analysis in this work, we begin by fitting an absorbed power-law model to the spectra, and then a multicolour disk blackbody model is added if it has a significance level above 99% based on the $F-$test (Table 1). Coincidentally, all observations performed in the PC mode have fewer photons, which can be fitted by the single power-law model. On the other hand, all WT mode data have high signal-to-noise ratios, and an additional disk blackbody component is required. Since we do not expect the absorption column density $N_{\rm H}$ to be different among the *Swift* observations, we also try to fit all PC mode data simultaneously with the same value of $N_{\rm H}$, but leave the power-law model parameters untied, yielding $N_{\rm H} = (2.7 \pm 0.5) \times 10^{21}{\rm cm}^{-2}$. Alternatively, we obtain $N_{\rm H} = (4.2 \pm 0.1) \times 10^{21}{\rm cm}^{-2}$ if modelling all WT mode observations with a common value of $N_{\rm H}$. It is worth to note that the value of $N_{\rm H}$ varies with adopted models; however, our results shown below are not dependent on the precise value of $N_{\rm H}$.

The UVOT data were taken in the image mode. In order to increase photon statistics, we stack the images when there is more than one exposure in the observations by using `uvotimsum`. An aperture radius 5 arcsec is adopted for the aperture photometry in the stacked images, and the background flux density is measured from a neighbouring source free sky region. We also estimate the 3σ upper limits if the source was undetected.

2.2. RXTE

The denser *RXTE* observations were executed to cover the activities of Swift J1842.5-1124, especially from 2008 September to November. In this work, we focus on data from the main instrument of *RXTE* — the Proportional Counter Array (PCA). The data from the PCU2 are filtered with the standard criteria: the Earth-limb elevation angle larger than 10° and the spacecraft pointing offset less than 0.02°. The bright and faint background models are used for creating background files when the source intensities were larger and lower than 40 count s^{-1} PCU^{-1}, respectively. We produce the background-subtracted light curves

[1] see http://swift.gsfc.nasa.gov/docs/heasarc/caldb/swift/docs/xrt/SWIFTXRT-CALDB-09.pdf

Obs.ID	MJD	$N_{\rm H}$ (10^{22} cm^{-2})	kT (keV)	Γ	Flux$_{\rm Po}$ (10^{-9}erg cm^{-2} s^{-1})	Flux$_{\rm Total}$ (10^{-9}erg cm^{-2} s^{-1})	χ^2/dof
00031234001§	54654.6	$0.30^{+0.16}_{-0.14}$	–	$1.50^{+0.24}_{-0.22}$	$0.27^{+0.02}_{-0.02}$	$0.27^{+0.02}_{-0.02}$	25.0/36
00031234002	54656.6	$0.55^{+0.16}_{-0.17}$	$0.12^{+0.02}_{-0.01}$	$1.64^{+0.11}_{-0.11}$	$0.28^{+0.01}_{-0.01}$	$0.35^{+0.12}_{-0.07}$	217.6/249
00031234003§	54657.3	$0.53^{+0.23}_{-0.20}$	–	$1.75^{+0.37}_{-0.33}$	$0.20^{+0.03}_{-0.02}$	$0.20^{+0.03}_{-0.02}$	14.9/19
00031234004§	54658.3	$0.26^{+0.12}_{-0.11}$	–	$1.24^{+0.22}_{-0.20}$	$0.19^{+0.02}_{-0.02}$	$0.19^{+0.02}_{-0.02}$	42.2/41
00031234005§	54659.9	$0.26^{+0.11}_{-0.10}$	–	$1.33^{+0.18}_{-0.17}$	$0.16^{+0.01}_{-0.01}$	$0.16^{+0.01}_{-0.01}$	48.7/52
00031234006§	54660.4	$0.22^{+0.08}_{-0.07}$	–	$1.23^{+0.14}_{-0.13}$	$0.16^{+0.01}_{-0.01}$	$0.16^{+0.01}_{-0.01}$	77.4/74
00324112000$^{\sharp}$	54717.3	$0.33^{+0.13}_{-0.10}$	$0.22^{+0.14}_{-0.05}$	$1.68^{+0.11}_{-0.13}$	$1.02^{+0.05}_{-0.05}$	$1.16^{+0.23}_{-0.11}$	198.0/187
00031234007	54720.8	$0.29^{+0.08}_{-0.04}$	$0.34^{+0.14}_{-0.12}$	$1.70^{+0.11}_{-0.13}$	$1.16^{+0.06}_{-0.08}$	$1.27^{+0.12}_{-0.05}$	355.6/301
00031234008	54721.7	$0.36^{+0.06}_{-0.04}$	$0.24^{+0.07}_{-0.05}$	$1.92^{+0.06}_{-0.06}$	$1.50^{+0.05}_{-0.05}$	$1.67^{+0.13}_{-0.08}$	434.0/398
00031234009	54722.5	$0.30^{+0.04}_{-0.02}$	$0.37^{+0.09}_{-0.09}$	$1.75^{+0.09}_{-0.10}$	$1.34^{+0.06}_{-0.07}$	$1.49^{+0.06}_{-0.04}$	321.5/324
00031234010	54730.6	$0.39^{+0.02}_{-0.01}$	$0.74^{+0.01}_{-0.01}$	$1.83^{+0.13}_{-0.15}$	$1.74^{+0.24}_{-0.22}$	$4.58^{+0.09}_{-0.07}$	597.1/552
00031234011	54751.1	$0.45^{+0.01}_{-0.01}$	$0.67^{+0.01}_{-0.01}$	$1.77^{+0.13}_{-0.14}$	$1.67^{+0.21}_{-0.18}$	$4.26^{+0.07}_{-0.06}$	760.4/525
00031234012	54752.8	$0.43^{+0.02}_{-0.02}$	$0.64^{+0.01}_{-0.01}$	$2.03^{+0.13}_{-0.14}$	$1.96^{+0.28}_{-0.25}$	$4.09^{+0.11}_{-0.10}$	574.5/496
00031234013	54765.9	$0.40^{+0.01}_{-0.01}$	$0.60^{+0.01}_{-0.01}$	$2.02^{+0.10}_{-0.11}$	$1.37^{+0.14}_{-0.13}$	$2.81^{+0.06}_{-0.05}$	531.1/543
00031234014	54779.2	$0.39^{+0.02}_{-0.02}$	$0.45^{+0.02}_{-0.03}$	$2.11^{+0.10}_{-0.11}$	$1.22^{+0.11}_{-0.11}$	$1.68^{+0.05}_{-0.04}$	497.4/418

Table 1. Best fit results for *Swift*/XRT observations. Flux$_{\rm Po}$: 0.6–10 keV unabsorbed flux for the power-law component. Flux$_{\rm Total}$: total unabsorbed flux calculated in 0.6–10 keV. §: Observations were operated in the photon-counting mode, and the rest of *Swift*/XRT observations were executed in the window-timing mode. $^{\sharp}$: There were two short automated observations (Obs IDs = 00324112000 and 00324116000) performed within two hours on 2008 September 14 (MJD = 54717); hence we fit them together in order to improve the signal-to-noise.

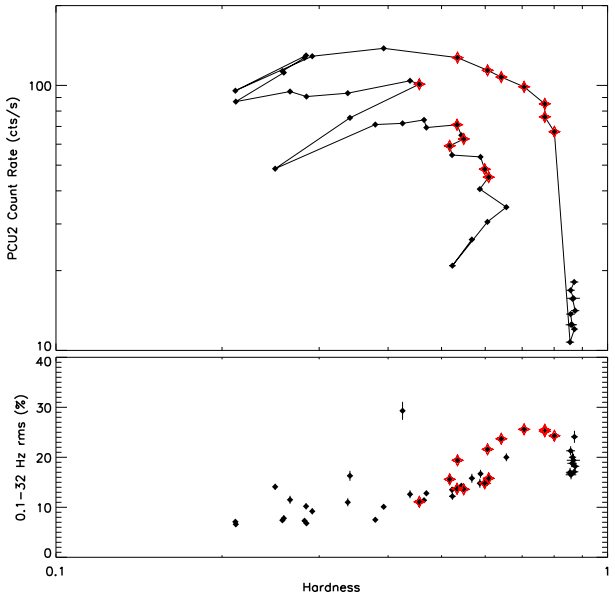

Fig. 2. Hardness-intensity diagram (HID: top panel) and hardness-rms diagram (HRD: bottom panel) for the 2008 outburst of Swift J1842.5-1124. The red symbols corresponds to the data in which QPOs were detected.

in the PCA channels of 8-14 (3.7–6.3 keV) and 15-25 (6.3–10.6 keV), then average their count rates in each observation and plot the HID in Figure 2. We first fit the PCA spectra with an absorbed power-law model, and then include an additional multicolour disk blackbody model when its significance is larger than 99%, as we did to the *Swift/XRT* data, while the neutral hydrogen column density in the PCA spectral fitting is fixed to 3.6×10^{21} cm^{-2} according to the *Swift*/XRT spectral fitting (Table 1). An absorption edge around 7 keV is also added to account for the line feature, and the recommended systematic error of 0.5% is applied. The fitting results are shown in Table 2.

Obs.ID	Frequency (Hz)	FWHM (Hz)	rms$_{\rm QPO}$
LHS to HSS			
93065-04-03-00	$0.85^{+0.01}_{-0.01}$	$0.14^{+0.02}_{-0.02}$	19.44±3.13
93065-04-04-00	$1.15^{+0.01}_{-0.01}$	$0.21^{+0.03}_{-0.03}$	21.27±3.06
93065-04-04-01	$1.36^{+0.01}_{-0.01}$	$0.22^{+0.03}_{-0.03}$	21.20±2.84
93065-04-04-02	$2.17^{+0.02}_{-0.02}$	$0.32^{+0.05}_{-0.04}$	21.80±3.17
93065-04-04-04	$3.07^{+0.02}_{-0.02}$	$0.35^{+0.05}_{-0.04}$	19.66±2.70
93065-04-04-03	$3.75^{+0.03}_{-0.03}$	$0.44^{+0.07}_{-0.06}$	18.17±2.86
93065-04-06-00	$5.31^{+0.03}_{-0.03}$	$0.58^{+0.07}_{-0.06}$	14.68±1.71
HSS to LHS			
93111-01-03-02	$7.98^{+0.31}_{-0.39}$	$1.45^{+1.55}_{-0.83}$	8.16±6.90
93111-01-05-02	$7.18^{+0.27}_{-0.30}$	$1.71^{+1.33}_{-0.80}$	12.12±7.25
93111-01-06-00	$7.12^{+0.11}_{-0.10}$	$0.81^{+0.51}_{-0.29}$	9.70±4.68
93111-01-06-01	$8.18^{+0.35}_{-0.25}$	$0.86^{+0.96}_{-0.57}$	8.80±8.69
93111-01-07-02	$6.13^{+0.18}_{-0.20}$	$0.79^{+0.80}_{-0.40}$	9.41±7.08
93111-01-08-00	$5.56^{+0.16}_{-0.19}$	$1.00^{+0.77}_{-0.47}$	11.14±6.68

Table 3. Log of QPOs.

The light curves in the channel of 0-43 (2–19 keV) are extracted from the PCA Event mode data, E_125us_64M_0_1s for temporal analysis. The data are divided into 32 s segments with 8 ms time bins, and the PDSs are generated with the task `powspec`. We adopt the Miyamoto method to normalize the PDSs (Miyamoto et al. 1991), and average them using a logarithmic rebinning. After subtracting the Poisson noise, we integrate the fractional root mean square (rms) in the 0.1–32 Hz, and plot the hardness-rms diagram (HRD) in the bottom panel of Figure 2. However, the low signal-to-noise ratio of data do not allow us to carry out energy-dependent studies, for example the energy dependence of the centroid frequency and phase lag of QPOs.

3. Results

Since the first X-ray observation was taken in 2008 July, the X-ray flux of Swift J1842.5-1124 declined exponentially with time

Obs.ID	MJD	kT (keV)	Γ	$\mathrm{Flux_{Po}}$ (10^{-9}erg cm^{-2} s^{-1})	$\mathrm{Flux_{Total}}$ (10^{-9}erg cm^{-2} s^{-1})	χ^2/dof
93065-04-01-00	54656.5	–	$1.55^{+0.03}_{-0.03}$	$0.37^{+0.01}_{-0.01}$	$0.37^{+0.01}_{-0.01}$	26.3/45
93065-04-01-01	54657.4	–	$1.59^{+0.03}_{-0.03}$	$0.34^{+0.01}_{-0.01}$	$0.34^{+0.01}_{-0.01}$	38.9/45
93065-04-02-00	54658.2	–	$1.60^{+0.05}_{-0.04}$	$0.32^{+0.01}_{-0.01}$	$0.32^{+0.01}_{-0.01}$	35.4/45
93065-04-02-01	54658.3	–	$1.57^{+0.03}_{-0.03}$	$0.33^{+0.01}_{-0.01}$	$0.33^{+0.01}_{-0.01}$	32.8/45
93065-04-02-02	54659.5	–	$1.57^{+0.03}_{-0.03}$	$0.30^{+0.01}_{-0.01}$	$0.30^{+0.01}_{-0.01}$	41.2/45
93065-04-02-03	54660.2	–	$1.57^{+0.04}_{-0.03}$	$0.28^{+0.01}_{-0.01}$	$0.28^{+0.01}_{-0.01}$	32.9/45
93065-04-02-04	54661.9	–	$1.57^{+0.04}_{-0.04}$	$0.27^{+0.01}_{-0.01}$	$0.27^{+0.01}_{-0.01}$	30.5/45
93065-04-02-05	54662.0	–	$1.61^{+0.05}_{-0.05}$	$0.25^{+0.01}_{-0.01}$	$0.25^{+0.01}_{-0.01}$	39.7/45
93065-04-02-06	54663.2	–	$1.60^{+0.03}_{-0.03}$	$0.25^{+0.01}_{-0.01}$	$0.25^{+0.01}_{-0.01}$	34.0/45
93065-04-02-07	54664.7	–	$1.59^{+0.03}_{-0.03}$	$0.23^{+0.01}_{-0.01}$	$0.23^{+0.01}_{-0.01}$	34.7/45
93065-04-03-00	54718.3	$1.59^{+0.11}_{-0.14}$	$1.51^{+0.06}_{-0.06}$	$1.20^{+0.04}_{-0.04}$	$1.32^{+0.01}_{-0.01}$	51.5/43
93065-04-04-00	54721.1	$1.60^{+0.10}_{-0.14}$	$1.54^{+0.07}_{-0.08}$	$1.23^{+0.04}_{-0.04}$	$1.45^{+0.01}_{-0.01}$	49.9/43
93065-04-04-01	54724.1	$1.61^{+0.13}_{-0.20}$	$1.64^{+0.08}_{-0.09}$	$1.49^{+0.08}_{-0.08}$	$1.59^{+0.01}_{-0.01}$	51.5/43
93065-04-04-02	54725.9	$1.35^{+0.12}_{-0.19}$	$1.77^{+0.06}_{-0.07}$	$1.65^{+0.06}_{-0.07}$	$1.78^{+0.01}_{-0.01}$	62.7/43
93065-04-04-04	54727.1	$1.17^{+0.17}_{-0.40}$	$1.95^{+0.07}_{-0.08}$	$1.70^{+0.07}_{-0.09}$	$1.82^{+0.01}_{-0.01}$	48.7/43
93065-04-04-03	54727.8	$1.03^{+0.14}_{-0.20}$	$2.04^{+0.04}_{-0.05}$	$1.74^{+0.05}_{-0.06}$	$1.86^{+0.01}_{-0.01}$	60.5/43
93065-04-06-00	54729.0	$0.72^{+0.09}_{-0.09}$	$2.19^{+0.03}_{-0.03}$	$1.84^{+0.02}_{-0.03}$	$1.98^{+0.01}_{-0.01}$	67.4/43
93065-04-06-01	54730.9	$0.70^{+0.03}_{-0.03}$	$2.35^{+0.04}_{-0.04}$	$1.58^{+0.02}_{-0.02}$	$1.97^{+0.01}_{-0.01}$	53.7/43
93065-04-06-02	54732.1	$0.69^{+0.01}_{-0.01}$	$2.40^{+0.05}_{-0.05}$	$1.15^{+0.02}_{-0.02}$	$1.75^{+0.01}_{-0.01}$	56.3/43
93065-04-06-04	54733.3	$0.69^{+0.01}_{-0.01}$	$2.12^{+0.09}_{-0.09}$	$0.59^{+0.02}_{-0.01}$	$1.28^{+0.01}_{-0.01}$	64.8/43
93065-04-06-03	54735.0	$0.72^{+0.02}_{-0.02}$	$2.26^{+0.08}_{-0.09}$	$1.08^{+0.03}_{-0.03}$	$1.71^{+0.01}_{-0.01}$	40.1/43
93065-04-05-00	54735.0	$0.71^{+0.01}_{-0.02}$	$2.31^{+0.07}_{-0.07}$	$1.06^{+0.02}_{-0.02}$	$1.72^{+0.01}_{-0.01}$	46.1/43
93065-04-05-01	54737.6	$0.70^{+0.01}_{-0.01}$	$2.30^{+0.06}_{-0.06}$	$0.86^{+0.02}_{-0.01}$	$1.52^{+0.01}_{-0.01}$	50.2/43
93111-01-01-00	54739.5	$0.67^{+0.01}_{-0.01}$	$2.35^{+0.05}_{-0.04}$	$0.89^{+0.01}_{-0.01}$	$1.51^{+0.01}_{-0.01}$	54.9/43
93111-01-01-01	54741.4	$0.68^{+0.01}_{-0.01}$	$2.10^{+0.07}_{-0.06}$	$0.56^{+0.01}_{-0.01}$	$1.18^{+0.01}_{-0.01}$	50.3/43
93111-01-02-00	54745.0	$0.67^{+0.02}_{-0.01}$	$2.22^{+0.06}_{-0.09}$	$0.76^{+0.01}_{-0.02}$	$1.31^{+0.01}_{-0.01}$	65.1/43
93111-01-02-02	54747.6	$0.65^{+0.01}_{-0.01}$	$2.30^{+0.06}_{-0.06}$	$0.79^{+0.01}_{-0.01}$	$1.26^{+0.01}_{-0.01}$	58.0/43
93111-01-03-00	54749.4	$0.67^{+0.02}_{-0.02}$	$2.27^{+0.05}_{-0.05}$	$0.94^{+0.01}_{-0.01}$	$1.32^{+0.01}_{-0.01}$	52.9/43
93111-01-03-01	54751.1	$0.66^{+0.04}_{-0.04}$	$2.32^{+0.05}_{-0.05}$	$1.29^{+0.02}_{-0.02}$	$1.52^{+0.01}_{-0.01}$	40.1/43
93111-01-03-02	54753.1	$0.64^{+0.04}_{-0.04}$	$2.28^{+0.03}_{-0.04}$	$1.31^{+0.02}_{-0.02}$	$1.51^{+0.01}_{-0.01}$	83.3/43
93111-01-03-03	54755.1	$0.58^{+0.03}_{-0.03}$	$2.43^{+0.08}_{-0.08}$	$0.79^{+0.01}_{-0.01}$	$1.06^{+0.01}_{-0.01}$	27.4/43
93111-01-04-00	54757.1	$0.61^{+0.01}_{-0.01}$	$2.14^{+0.06}_{-0.06}$	$0.38^{+0.01}_{-0.01}$	$0.69^{+0.01}_{-0.01}$	36.2/43
93111-01-04-01	54759.2	$0.62^{+0.02}_{-0.02}$	$2.30^{+0.04}_{-0.04}$	$0.80^{+0.01}_{-0.01}$	$1.03^{+0.01}_{-0.01}$	40.6/43
93111-01-04-03	54761.9	$0.53^{+0.05}_{-0.04}$	$2.45^{+0.05}_{-0.06}$	$0.89^{+0.01}_{-0.01}$	$1.03^{+0.01}_{-0.01}$	26.8/43
93111-01-05-00	54763.3	$0.56^{+0.04}_{-0.04}$	$2.34^{+0.03}_{-0.03}$	$0.99^{+0.01}_{-0.01}$	$1.10^{+0.01}_{-0.01}$	32.3/43
93111-01-05-01	54765.8	$0.53^{+0.04}_{-0.04}$	$2.33^{+0.04}_{-0.04}$	$0.93^{+0.01}_{-0.01}$	$1.04^{+0.01}_{-0.01}$	38.0/43
93111-01-05-02	54767.5	$0.50^{+0.08}_{-0.07}$	$2.28^{+0.03}_{-0.04}$	$1.03^{+0.01}_{-0.01}$	$1.09^{+0.01}_{-0.01}$	39.2/43
93111-01-05-03	54769.6	$0.60^{+0.12}_{-0.12}$	$2.20^{+0.05}_{-0.05}$	$0.96^{+0.01}_{-0.02}$	$1.02^{+0.01}_{-0.01}$	43.4/43
93111-01-06-00	54772.2	$0.47^{+0.06}_{-0.06}$	$2.23^{+0.02}_{-0.02}$	$0.93^{+0.01}_{-0.01}$	$0.98^{+0.01}_{-0.01}$	37.8/43
93111-01-06-01	54774.0	$0.57^{+0.08}_{-0.08}$	$2.25^{+0.06}_{-0.06}$	$0.83^{+0.01}_{-0.01}$	$0.90^{+0.01}_{-0.01}$	54.0/43
93111-01-06-02	54776.1	$0.49^{+0.07}_{-0.07}$	$2.27^{+0.04}_{-0.05}$	$0.78^{+0.01}_{-0.01}$	$0.84^{+0.01}_{-0.01}$	25.6/43
93111-01-07-00	54778.3	$0.42^{+0.12}_{-0.11}$	$2.17^{+0.03}_{-0.03}$	$0.83^{+0.01}_{-0.01}$	$0.83^{+0.01}_{-0.01}$	24.9/43
93111-01-07-02	54782.8	$0.33^{+0.12}_{-0.11}$	$2.15^{+0.03}_{-0.03}$	$0.76^{+0.01}_{-0.01}$	$0.79^{+0.01}_{-0.01}$	40.7/43
93111-01-08-00	54786.0	$0.57^{+0.21}_{-0.19}$	$2.11^{+0.03}_{-0.04}$	$0.72^{+0.01}_{-0.01}$	$0.74^{+0.01}_{-0.01}$	34.2/43
93111-01-08-01	54789.5	$0.43^{+0.13}_{-0.12}$	$2.18^{+0.05}_{-0.05}$	$0.62^{+0.01}_{-0.01}$	$0.64^{+0.01}_{-0.01}$	24.9/43
93454-01-01-00	54794.0	$0.76^{+0.36}_{-0.43}$	$2.00^{+0.05}_{-0.07}$	$0.57^{+0.01}_{-0.02}$	$0.58^{+0.01}_{-0.01}$	25.1/43
93454-01-02-00	54798.4	$0.22^{+0.09}_{-0.16}$	$2.17^{+0.03}_{-0.04}$	$0.48^{+0.01}_{-0.01}$	$0.49^{+0.01}_{-0.01}$	36.9/43
93454-01-02-01	54802.4	$0.55^{+0.09}_{-0.09}$	$2.10^{+0.10}_{-0.11}$	$0.29^{+0.01}_{-0.01}$	$0.33^{+0.01}_{-0.01}$	27.3/43
93454-01-02-02	54803.3	$0.53^{+0.14}_{-0.13}$	$2.15^{+0.07}_{-0.08}$	$0.39^{+0.01}_{-0.01}$	$0.40^{+0.01}_{-0.01}$	34.8/43

Table 2. Best fit results for *RXTE*/PCA data with the absorption column density fixed to 3.6×10^{21} cm^{-2}.

and became undetectable two weeks later. After a few days, the source re-brightened and reached the X-ray peak around the end of September (MJD ~ 54730, Figure 1). At the peak of outburst, the 0.6–10 keV X-ray flux estimated from the *Swift*/XRT observations were even higher than the 3-25 keV flux measured by *RXTE*/PCA, that is the X-ray spectra were relatively softer (Tables 1 and 2). However, the source was sparsely detected in the NUV bands (UW1, UM2, and UW2) around the peak of outburst. The flux density measured by the V filter remained nearly constant ~ 0.26 mJy (with a slightly increase on MJD 54753) as the X-ray luminosity varied. Alternatively, the source was observed in the U band six times, and there was a weakly positive correlation between the U-band flux density and the X-ray flux with the Spearman's rank correlation coefficient of $\rho/P = 0.60/0.21$. In Figure 3, we plot the optical/NUV flux density versus the corresponding X-ray flux detected by *Swift*. Using the relation between the optical extinction and the hydrogen column density given by (Güver & Özel 2009), we find that the optical and NUV flux measured by each filter (~ 10^{-12} erg cm^{-2} s^{-1}) is smaller than the X-ray flux by about three orders of magnitude.

In the HID, Swift J1842.5-1124 displayed a 'q' shaped diagram, travelling counterclockwise from the bottom right corner with an additional excursion to a harder state and back in

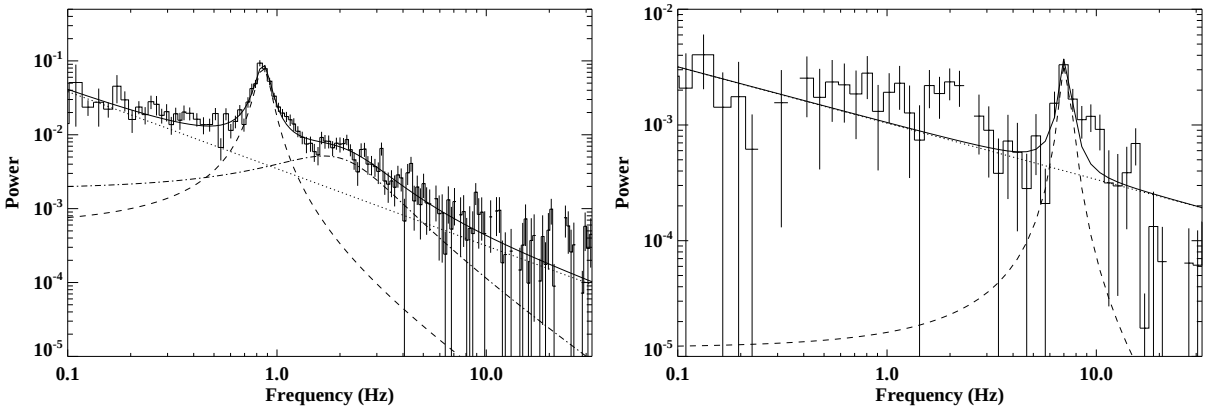

Fig. 4. Left panel: PDS for MJD 54718.3 (Obs ID = 93065-04-03-00) is fitted by a power-law plus two Lorentzian models. Right panel: PDS for MJD 54772.2 (Obs ID = 93111-01-06-00) is fitted by a power-law model with an additional Lorentzian component. We note that the PDS is rebinned for clarity.

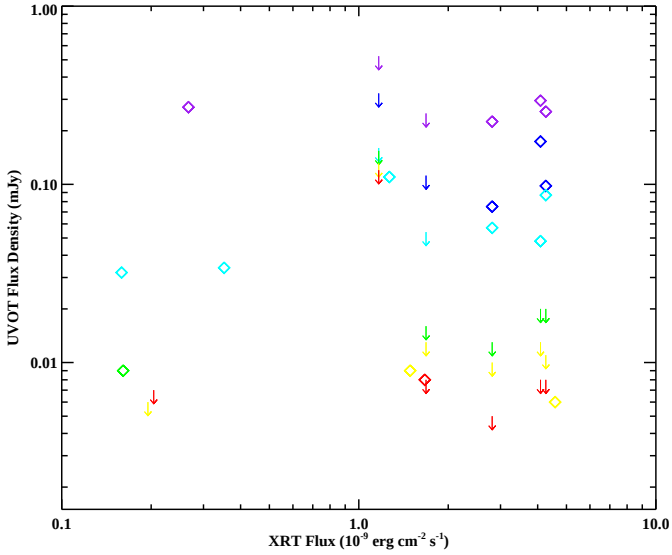

Fig. 3. Correlation between the optical/NUV flux density and the X-ray 0.6–10 keV flux. The meaning of different colours is the same as in the bottom panel of Figure 1. We do not plot the errors of data for clarify; while readers can find them in Figure 1.

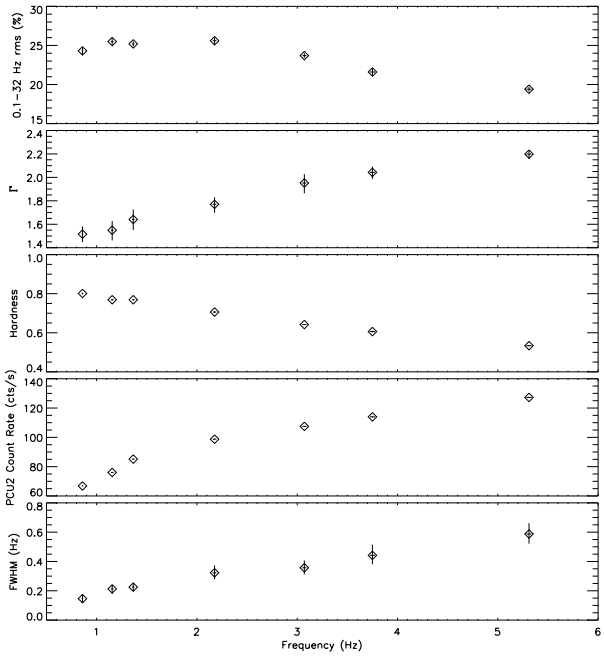

Fig. 5. Panels from top to bottom show the total fractional rms, photon index Γ, hardness, intensity, and the FWHM plotted against the QPO frequency, respectively.

2008 October (Figure 2). On the other hand, the total fractional rms generally decreased with the increasing hardness, and no hysteresis was observed in the HRD. That is, both the HID and HRD of Swift J1842.5-1124 resembled those found in other BH XRBs (e.g. Dunn et al. 2010; Motta et al. 2011; Zhou et al. 2013). Therefore, following the state definition described in Belloni & Motta (2016), we suggest that Swift J1842.5-1124 went through the LHS (the bottom right corner in the HID), the HIMS (the upper right corner), the HSS (the upper left corner), and then returned the LHS via the SIMS/HIMS during its 2008 outburst. In addition to the hardness and timing properties shown in the HID and HRD, the state identifications are supported by more detailed spectral fitting results (Tables 1 and 2) and timing analysis. The harder X-ray spectra accompanied by the strong aperiodic variabilities were observed in the LHS, while the larger values of photon index and weaker variabilities were found when the source transited to the HSS. Compared to the transition from the LHS to the HSS, the transition from the HSS to the LHS exhibited softer spectra with a photon index $\Gamma \sim 2.0 - 2.2$ (Table 2), that is the hysteresis.

A strong QPO with a frequency of $\sim$ 0.8 Hz had been reported by (Markwardt et al. 2008), and a weak QPO at $\sim$ 8 Hz presented on 2008 October 14 (MJD = 54753) was also suggested (Krimm et al. 2013). In this paper, we employ the power-

law and Lorentzian models in the PDSs fitting. The strong QPOs were revealed in the seven observations when the source transited from the LHS to the HSS; while the weak QPOs were displayed in the PDSs of another six observations during the source returned to LHS (Figure 2). As examples for both cases, we plot the PDSs with the data collected on 2008 September 9 (MJD = 54718.3) and November 2 (MJD = 54772.2) in Figure 4. The amplitude of QPO is calculated in the way of $rms_{\rm QPO} = (\pi \times LW \times LN)^{1/2}$, where LW is the full width half-maximum (FWHM) of the QPO, and LN is the normalization of Lorentzian component for QPO. The parameters of QPOs are listed in Table 3. Because of the large uncertainties, we cannot describe the final six marginal QPO features in detail, and we investigate only the first seven strong QPOs. The frequencies of these QPOs were not only correlate with the intensity but also anti-correlated with the hardness (Figure 5). In addition, the photon index Γ and the quality factor monotonically increased as the QPO frequency increased from 0.85 Hz to 5.31 Hz.

4. Discussion

It has been suggested that optical and NUV emissions in XRBs could stem from different components (e.g. Rykoff et al. 2007; Weng & Zhang 2015). The modest correlation between the U band and the X-ray fluxes (Figure 3) implies that the U band and the X-ray radiations have some connection via the X-ray reprocessing or the tail of outer disk thermal emission. Meanwhile, the emission at longer wavelengths does not show a significant correlation with the X-ray radiation, pointing to some other contribution (e.g. the companion star or jet). In particular, the U-band flux almost halved while the B-band flux enhanced by a factor of $\sim$ 1.8, when the source took an excursion in the HID (from MJD 54750 to 54755) (Figure 1). At this time, the thermal and non-thermal components have the comparable contribution to the (0.6–10 keV) X-ray emission. Coincidentally, a weak QPO was detected on MJD 54753; however, the low data statistic means that we cannot classify it. The positions in the HID and HRD indicate that the source transited between the HIMS and the SIMS (crossed the jet line), which could be associated to type-B QPOs and the launch of relativistic jet (see e.g. Figure 1 in Kylafis & Belloni 2015). If the jet produces part of the optical emissions, especially at long wavelengths, the reverse trends shown at the shorter (U) and longer (B) bands can be explained.

Since early 2008 September, the X-ray spectra became softer with Γ increasing from $\sim$ 1.5 to $\sim$ 2.4, indicating that Swift J1842.5-1124 started to transit from the LHS to HSS (via the HIMS). In the meantime, the prominent QPO features were observed in the seven observations. In addition to the position in the HID, the QPO frequencies, the high amplitude of QPO, and the flat-top noise component displayed in the profiles of PDSs (left panel of Figure 4) allow us to identify these QPOs as the type-C QPOs.

Various approaches have been made to further our understanding of evolution of low frequency QPOs in BH XRBs (see e.g. Tagger & Pellat 1999; Titarchuk & Fiorito 2004; Yan et al. 2013). The truncated disk model considering the Lense-Thirring precession had been proposed to explain the low frequency QPOs (e.g. Ingram et al. 2009), and now has been developed to interpret the simultaneous observation of both high frequency and low frequency QPOs (Motta et al. 2014; Fragile et al. 2016). In this model, the QPO frequency is expected to increase as the truncation radius moves in. Because of the low sensitivity of *RXTE*/PCA at below 2 keV, we cannot put a constraint on the disk radius. Moreover, the irradiation effect at the LHS would lead to an underestimate of disk radius, resulting in more uncertainties (e.g. Gierliński et al. 2008). Alternatively, when the source transited from the LHS to the HSS, the centroid frequencies of the observed type-C QPO monotonically increased with increasing intensity and decreasing hardness. The level of fast variability became lower and the photon index Γ also softened, from 1.51 to 2.19 (Figure 5). All these correlations imply a decreasing truncation radius and agree with the prediction of the Lense-Thirring precession model.

Acknowledgements. We thank the referee for helpful comments that improved this work. This work is supported by the National Natural Science Foundation of China under grants 11303022, 11133002, 11473023, 11543008, 11573023, 11173016 and 11433005, and by the Special Research Fund for the Doctoral Program of Higher Education (grant No. 20133207110006).

References

Altamirano, D., & Méndez, M., 2015, MNRAS, 449, 4027
Belloni, T. M., & Motta, S. E., 2016, arXiv:1603.07872
Belloni, T. M., Homan, J., Casella, P., et al. 2005, A&A, 440, 207
Casella, P., Belloni, T., & Stella, L. 2005, ApJ, 629, 403
Chen, W., Shrader, C. R., & Livio, M. 1997, ApJ, 491, 312
Coriat, M., Fender, R. P., & Dubus, G., 2012, MNRAS, 424, 1991
Corral-Santana, J. M., Casares, J., Muñoz-Darias, T., et al. 2016, A&A, 587, 61
Dunn, R. J. H., Fender, R. P., Körding, E. G., Belloni, T., Cabanac, C., 2010, MNRAS, 403, 61
Fender, R. P., Belloni, T. M., & Gallo, E., 2004, MNRAS, 355, 1105
Fragile, P. C., Straub, O., & Blaes, O., 2016, arXiv:1602.08082
Gehrels, N., Chincarini, G., Giommi, P., et al. 2004, ApJ, 611, 1005
Gierliński, M., Done, C., & Page, K. 2008, MNRAS, 388, 753
Güver, T., & Özel, F., 2009, MNRAS, 400, 2050
King, A. R., & Ritter, H., 1998, MNRAS, 193, L42
Krimm, H. A., Holland, S. T., Corbet, R. H. D., et al. 2013, ApJS, 209, 14
Krimm, H. A., Kennea, J., Barthelmy, S. D., et al. 2008, ATel, 1610
Kylafis N. D., & Bellnoi, T. M., 2015, A&A, 574, A133
Lasota, J. P. 2001, New Astron. Rev., 45, 449
Li, Z. B., Qu, J. L., Song, L. M., et al. 2013, MNRAS, 428, 1704
Markwardt, C. B., Halpern, J. P., Holland, S. T., et al. 2008, ATel, 1716
Miller, J. M., Homan, J., Steeghs, D., et al. 2006, ApJ, 653, 525
Miyamoto, S., Kimura K., & Kitamoto, S., 1991, ApJ, 383, 784
Motta, S. E., Belloni, T. M., Stella, L., et al. 2014, MNRAS, 437, 2554
Motta, S. E., Muñoz-Darias, T., Casella, T., et al. 2011, MNRAS, 418, 2292
Ingram, A., & Done, C., 2011, MNRAS, 415, 2323
Ingram A., Done C., & Fragile P. C., 2009, MNRAS, 397, L101
Qu, J. L., Lu, F. J., Song, L. M., et al. 2010, ApJ, 710, 836
Reig, P., & Kylafis, N. D., 2015, A&A, 584, 109
Remillard, R. A., & McClintock, J. E. 2006, ARA&A, 44, 49
Roy, J., Agrawal, P. C., Paul, B., & Duorah, K. 2011, MNRAS, 412, 1011
Rykoff, E. S., Miller, J. M., Steeghs, D., & Torres, M. A. P., 2007, ApJ, 666, 1129
Soleri, P., Bellnoi, T. M., & Casella, P., 2008, MNRAS, 383, 1089
Stella, L., & Vietri, M., 1998, ApJL, 492, L59
Tagger, M., & Pellat, R. 1999, A&A, 349, 1003
Tetarenko, B. E., Sivakoff, G. R., Heinke, C. O., et al. 2015, ApJS, 222, 15
Titarchuk, L. G., & Fiorito, R. 2004, ApJ, 612, 988
van Paradijs J., & McClintock J. E., 1994, A&A, 290, 133
Varnière, P., Tagger, M., & Rodriguez, J. 2012, A&A, 545, A40
Veledina, A., Revnivtsev, M. G., Durant, M., et al. 2015, MNRAS, 454, 2855
Weng, S.-S., & Zhang, S.-N., 2015, MNRAS, 447, 486
Yan, Z., & Yu, W. F., 2015, ApJ, 805, 87
Yan, S. P., Wang, N., Ding, G. Q., et al. 2013, ApJ, 767, 44
Zhou, J. N., Liu, Q. Z., Chen, Y. P., et al. 2013, MNRAS, 431, 2285
Zhang 2013, FrPhy, 8, 630